A dynamical feedback model for adaptation in the olfactory transduction pathway - Supporting Material

April 24, 2012

1 Experimental Methods

Patch clamp experiments on dissociated olfactory sensory neurons Olfactory sensory neurons were dissociated from the olfactory epithelium of newts (*Cynops pyrrhogaster*) as described in [12, 13], salamanders (*Ambystoma tigrinum*) as in [7] or mice (BALB/c strain) as in [14]. All experiments were carried out in accordance with the Italian Guidelines for the Use of Laboratory Animals (Decreto Legislativo 27/01/1992, no. 116). Olfactory sensory neurons were identified by their characteristic bipolar shape and only neurons with clearly visible cilia were used for the experiments. Currents were measured in the whole-cell voltage-clamp mode as previously described [13, 7, 14]. Transduction currents were elicited by odorant, IBMX, the photorelease of cAMP [13, 2] or its non-hydrolyzable form 8-Br-cAMP [2], and were recorded at a holding potential of -50 mV. IBMX was dissolved in DMSO at 100 mM and an aliquot was added to the Ringer solution to obtain a final concentration of 0.1 mM. IBMX was applied to the neurons through a glass micropipette by pressure ejection (Picospritzer, Intracel, United Kingdom). All experiments were performed at room temperature.

Photolysis of Caged Compounds Caged cAMP (Dojindo, Japan) and BCMCM-8-Br-cAMP (provided by V. Hagen, Leibniz-Institut fur Molekulare Pharmakologie, Berlin, Germany, [2]) were dissolved in DMSO. Final concentrations were obtained by diluting an aliquot of the stock solution into the pipette solution. Caged compounds diffused into the neuron through the patch pipette and cyclic nucleotides were photoreleased by ultraviolet flashes applied to the ciliary region through the epifluorescence port of the microscope [13, 2]. For the experiments in the newt the light source was a 100W mercury lamp. Timing and duration of the flash were regulated by a mechanical shutter as described in [13]. For the experiments performed in the mouse the light source was a xenon flash-lamp JML-C2 system (Rapp OptoElectronic, Hamburg, Germany) that allowed an intense and short light flash (about 1.5 ms), as described in [2].

2 Model

The transduction pathway Olfactory transduction occurs in the cilia of OSNs (Fig. 1). OSNs are bipolar neurons with an axon, soma, dendrite, and several cilia protruding from the apical side of the dendrite [11, 20]. The binding of an odorant molecule to an odorant receptor on a cilium induces a conformational change of the receptor causing the activation of an interacting G-protein. In turn, the G-protein stimulates the enzymatic activity of an adenylyl cyclase (AC) generating an increase in the concentration of cyclic AMP (cAMP). Cyclic nucleotide-gated (CNG) channels located in the ciliary membrane are directly activated by cAMP, causing a depolarizing influx of Na and Ca ions. The intracellular increase of Ca concentration directly gates Ca-activated Cl channels. Since OSNs maintain an unusually high internal concentration of Cl, which is in the same range as the Cl concentration present in the mucus at the external side of the ciliary membrane, the opening of Ca-activated Cl channels causes an efflux of Cl ions from the cilia, corresponding to an inward current that further contributes to the depolarization of OSNs [11, 17]. The depolarization spreads passively to the dendrite and soma of the neuron, triggering action potentials that are conducted along the axon to the olfactory bulb. Several Ca-dependent feedback mechanisms may contribute to adaptation. The cilia contain a phosphodiesterase that, after being activated by the complex Ca-Calmodulin (CaCaM), hydrolyzes cAMP [4]. The complex CaCaM and possibly other Ca-binding proteins decrease the sensitivity of the CNG channel to cAMP [1, 5, 6]. The activation of CaCaM-dependent protein kinase II (CaMK) inhibits AC activity [22]. Finally, the intracellular Ca concentration is reduced by Ca-extrusion through a Na/Ca exchanger [15]. The cilia contain only two types of ion channels, CNG and Ca-activated Cl channels. Voltage-gated channels are instead located in other compartments of OSNs: dendrite, soma and axon. The depolarization originating in the cilia spreads to the soma where action potentials originate and carry the information to the olfactory bulb [11, 20]. Here, we study the transduction current in voltage-clamp conditions to isolate the transduction properties of the cascade from voltage-gated channels. The generation of action potentials occurring at the soma and spike rate adaptation depends also on the specific properties of the voltage-gated channels expressed by OSNs and are not modeled here. However, it is worth noting that adaptational properties have also been measured in OSNs in vivo in some pioneering studies, as reviewed by Getchell [8]. Both the generator potential measured using electroolfactograms in frogs [16] and single unit extracellular recordings from salamander OSNs [9] exhibited step adaptation and multipulse adaptation in response to odorants. These results indicate that the choice of the transduction current as the output of OSNs is also a good representation of the response of OSNs in natural conditions.

Description of the reactions As stated in the main text, of the 5 state variables of the model, we impose mass conservation on the 3 proteins: CNG channels, calmodulin and Ca-binding protein. No mass conservation is imposed on cAMP and Ca ions. Since Ca:cAMP:CaM have molecular weights 40:329:16800, this assumption is reasonable: small molecules can diffuse more rapidly in the cytoplasm of the neuron. In addition Ca and cAMP cannot be conserved because they are also involved in non-conservative reactions: Ca can enter the cell through the CNG channels, can diffuse away from the internal membrane and can be extruded through Na/Ca exchangers; cAMP can be hydrolyzed by PDE.

Most of the terms appearing in Eqs (1)-(7) in the main text are derived from mass action kinetics. We report here the corresponding reactions:

$$2\ \mathrm{cAMP} + \mathrm{CNG_c} \underset{\lambda_1}{\overset{\gamma_1}{\rightleftharpoons}} \mathrm{CNG_o}$$
$$\mathrm{Ca} + \mathrm{BP} \underset{\lambda_2}{\overset{\gamma_2}{\rightleftharpoons}} \mathrm{CaBP}$$
$$2\ \mathrm{Ca} + \mathrm{CaM} \underset{\lambda_3}{\overset{\gamma_3}{\rightleftharpoons}} \mathrm{CaCaM}$$

where

$$\begin{aligned} \mathrm{CNG_c} + \mathrm{CNG_o} &= \mathrm{CNG_{tot}}; \\ \mathrm{BP} + \mathrm{CaBP} &= \mathrm{BP_{tot}}; \\ \mathrm{CaM} + \mathrm{CaCaM} &= \mathrm{CaM_{tot}}. \end{aligned}$$

The other terms in the ODEs represent the degradation rates for cyclic AMP and Ca (representing their diffusion and, for Ca, the extrusion through the Na/Ca exchanger) and the (non-mass-action) term representing Ca influx due to the opening of the CNG channels. The model is completed by the two feedback terms. The first one reproduces the CaCaM-dependent activation of PDE which hydrolyzes cAMP into AMP. This was difficult for us to represent through mass action kinetics due to the lack in our model of a variable representing the adenylyl cyclase responsible in the biological pathway for the regeneration of cAMP. The second feedback term represents the action of the CaBP complex on the CNG channels: in this case the binding protein BP is natively and permanently bound to the channel and it remains "silent" as long as Ca concentration is low. Upon arrival of Ca and its binding with BP, the complex CaBP activates the closing gate of the channel. In Eq. (1) of the paper this is represented as a negative term which "competes" with the positive term (gate opening induced by cAMP) thereby reducing the sensitivity of the channel to cAMP. An alternative model for this feedback action is presented in Section 3 of this Supplementary Information.

Choosing the pre-stimulus baseline level For some of the quantities of interest in our model, ranges of plausible values of basal (pre-stimulus) concentrations in the olfactory cilia are available. This concerns in particular cAMP and Ca. For cAMP, the literature reports a basal concentration of $\sim 0.1\mu$M [4, 18] and a peak of concentration $\sim 100\mu$M during the response to a stimulus [21]. We used this information to normalize the value of cAMP in our simulation so that the magnitude of the transient never exceeds a 10^3 ratio with respect to its basal value (for reasonable values of the parameters, not necessarily for the optimal set). Knowing the ratio of the output current before/after a stimulus allows us to choose a proper initial value for Ca and for $\mathrm{CNG_o}$ compatible with the data. As for the other state variables, plausible values can easily be chosen, assuming that at steady state (without input), the feedbacks are nearly inactive. Once the parameters are chosen, to avoid spurious prestimulus transients in the simulations of the paper, the initial condition of the state variables is set equal to the steady state reached by the system in correspondence of u=0.

Modeling the input stimulus The shape of the input u in Eq. (1) for cAMP changes with the type of stimulation considered. We reported in Fig. S1 and in Table S1 the shape and the parameter values for the different simulated inputs. The plot of the profiles can be seen above those of the state variables in Fig. 2, S3 and S4. For odorant molecules and caged compounds, we chose a step-like function to represent the shape of the input, assuming fast kinetics for both release and termination of the stimulation. We imposed a total inhibition of the action of PDE in the data obtained using 8-Br-cAMP (the CaCaM feedback gain $k_1 = 0$ in this case). To model the

experimental data with IBMX as input, we instead used a ramp-like form for input onset and offset, because of the different mechanism of stimulation: IBMX suppresses part of the basal activity of PDE, directly leading to an increasing amount of cAMP. For this type of data the rise is steeper than the decay, with a rise duration equal to 0.02 s (corresponding to the experimental duration of the stimulus) and a decreasing duration equal to 2 s for the stimulation representing multipulse adaptation, while we used a 0.02 s increase followed by a constant amplitude, and by a 2 second-ramp decrease to represent the longer stimuli (see Fig. S1 and Table S1 for details). Furthermore a dedicated parameter B was added in the fitting procedure to represent the relative inhibition of the CaCaM feedback due to the action of the PDE (the parameter k_1 in the equations was multiplied by 1-B). The ∼75% inhibition of PDE by IBMX obtained by the parameter estimation seems to be a reasonable value and gives a good fit to the experimental data. A delay of the response, varying between 0.2 and 1 s, was added to represent the latency (in this case considered as the time required by the first part of the transduction process, upstream of cAMP production) in the fit of the responses to odorants or to IBMX. Such a delay was not added to the input profile for experiments using caged compounds, in which the photorelease of cyclic nucleotides is very fast and produced a rapid response (Fig. 3).

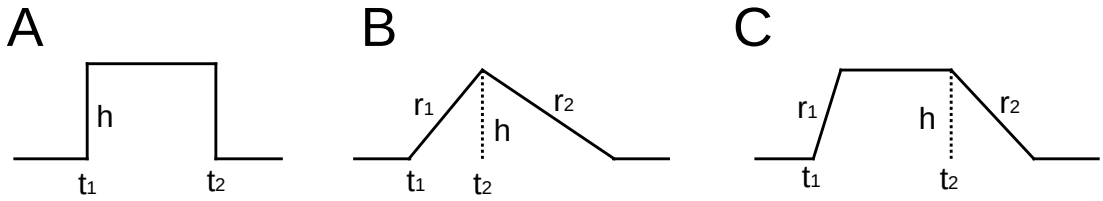

Figure S1: **Profiles of the shapes of the simulated inputs.** The profile A is used to simulate the response to odor, cAMP and 8-Br-cAMP, B is for the IBMX pulses, and C for the sustained stimuli of IBMX.

Table S1: Details of the simulated inputs. The shape corresponds to one of the three profiles represented in Fig. S1. h represents the amplitude of the stimulus, r_1 and r_2 represent the slopes of the profiles. All the time units are expressed in s.

	type	shape	h	(t2-t1)	delay	r_1	r_2
odor	pulses	A	200	0.2	0.2		
	sustained	A	100	43.5	1		
cAMP	pulses	A	300	0.1	0		
8-Br-cAMP	pulses	A	3000	0.005	0		
IBMX	pulses	B	140	0.02	0.3	7000	70
	sustained	C	50	24	1	2500	25
	sustained double	C	50	8	0.7	2500	25

Parameters estimation The parameters used in the model are listed in Table of the paper. In the equations for the current calculation (Eqs (8)-(9)), some of the parameters can be considered

constant: $I_{max} = 1$ because of the current normalization; the exponent 2 represents the cooperativity of I_{Cl} [2, 11]; and $k_c = 0.2$ to reproduce a relative contribution of $\sim 20\%$ of the I_{CNG} in the total current [3, 10].

The experiments depicted in Figs. 2, 3, 4 were performed in different experimental conditions and therefore we subdivided them into 4 subsets, each corresponding to a choice of input stimulus (odorant, caged cAMP, 8-Br-cAMP and IBMX), and fitted 4 distinct sets of parameters. The fit was performed normalizing the amplitudes of the current responses. The starting point of the whole fitting procedure was a collection of experimental data obtained using 8-Br-cAMP stimulations of increasing amplitude, in positive potential conditions (thus with a reduced inflow of Ca, if any, hence approximately in "open-loop" conditions) [2], see Fig. S2. In this way it was possible to obtain a good estimation of the association rate of cAMP and CNG channels, in our model represented by γ_1, of the corresponding dissociation constant λ_1 and of the degradation rate of cAMP δ_1. The input pulse amplitude and shape were assumed to be the same as those used in fitting the 8-Br-cAMP responses. Parameter values resulting from this fit were then used as the initial guesses for subsequent estimation of these parameters. The parameters were allowed to span from 0 to infinity with some exceptions: the intervals for the values of δ_1, λ_1 and γ_1 were restricted around the values previously found, and a lower bound equal to 0.1 was chosen for λ_2 and λ_3 to allow a complete recovery from adaptation of the response in about 30 seconds [2]. The other constrained parameter was $k_{1/2}$ appearing in the calculation of the chloride current: following the experimental data of [2, 11] it was allowed to vary between 2 and 5. The parameter B representing the relative inhibition of PDE due to the action of IBMX (see "Modeling the input stimulus" above for details) was considered only for the data obtained using IBMX, and was allowed to span from 0.6 to 1. All this a priori knowledge is reported in Table of the main text. Fits were performed using these initial values and constraints with the MATLAB function lsqcurvefit, which performs non-linear least squares (with a trust-region-reflective algorithm) simultaneously over the time series of each of the 4 experimental setups. The lsqcurvefit function finds the vector of coefficients $\mathbf{p}$ that optimizes the following functional

$$J^* = \min_{\mathbf{p}} ||F(\mathbf{p}, \mathbf{t}) - \mathbf{y}||_2{}^2 = \min_{\mathbf{p}} \sum_i (F(\mathbf{p}, t_i) - y_i)^2 ,$$

where $\mathbf{t}$ represents the time vector, $\mathbf{y}$ the experimental data, and $F(\mathbf{p},\mathbf{t})$ the output of our model. Table of the paper contains the numerical values obtained for the 4 experimental conditions.

Parameters estimation -Common fit for all experimental data We also took an alternative approach in which we compute a single parameter set for all experimental data. All the current time courses presented in the paper were used simultaneously to estimate numerical values for the parameters of Table of the paper ("common" column) using the same procedures described above. In Fig. S5, S6 and S7 the corresponding fits are shown for the experimental data of Fig. 2, 3, 4 of the paper. Overall, these new fits are still qualitatively accurate, although less precise than those shown in the paper. Notice in particular how the amplitude of the peaks on the double pulse experiments are less precise.

Evaluation of the goodness of the fit We performed several tests to evaluate the goodness of the parameter estimation.

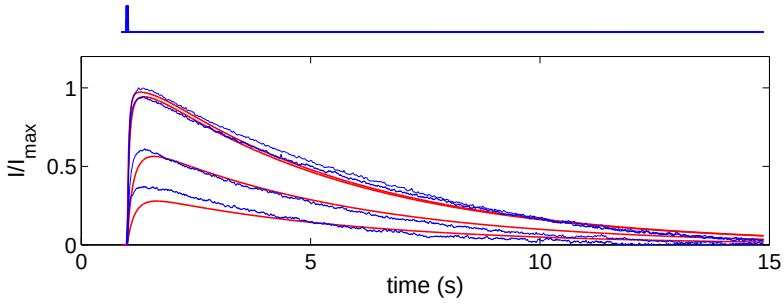

Figure S2: **Response to photorelease of caged cyclic nucleotides in a low Ca experiment.** The experimental data are shown in blue, the response of the model in red. The blue traces above the data represent the experimental stimulus. Response of a mouse OSN to photorelease of 8-Br-cAMP with ultraviolet light flashes of 1.5 ms at various relative intensities (0.25, 0.4, 0.8 and 1), recording at +50mV in Ringer solution. Parameter estimates: $\delta_1 = 2.28$, $\lambda_1 = 0.21$, $\gamma_1 = 0.09$. Experimental data from [2], reproduced with permission.

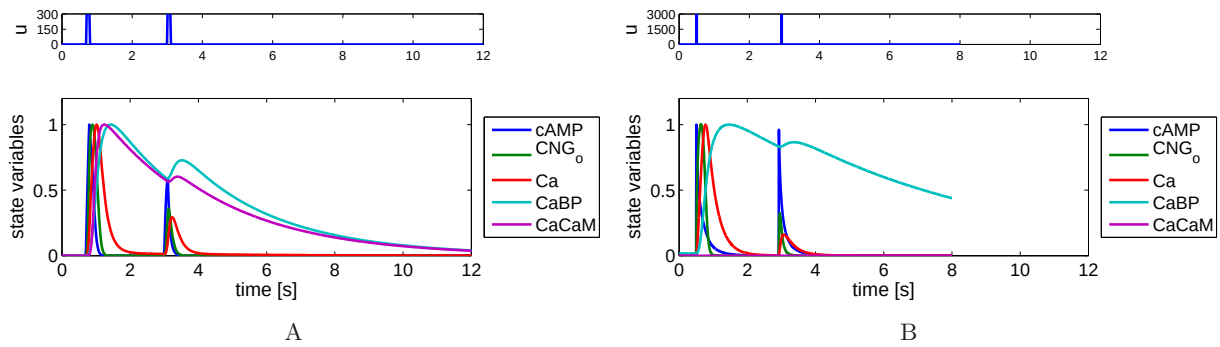

Figure S3: **Time profile of the state variables for the simulated data in response to caged compounds.** Panels (A) and (B) show the normalized simulation of the model in response to a paired-pulse stimulation using respectively caged cAMP and caged 8-Br-cAMP, corresponding to Fig. 3 of the main paper. For both figures, the upper panel represents the input given to the model.

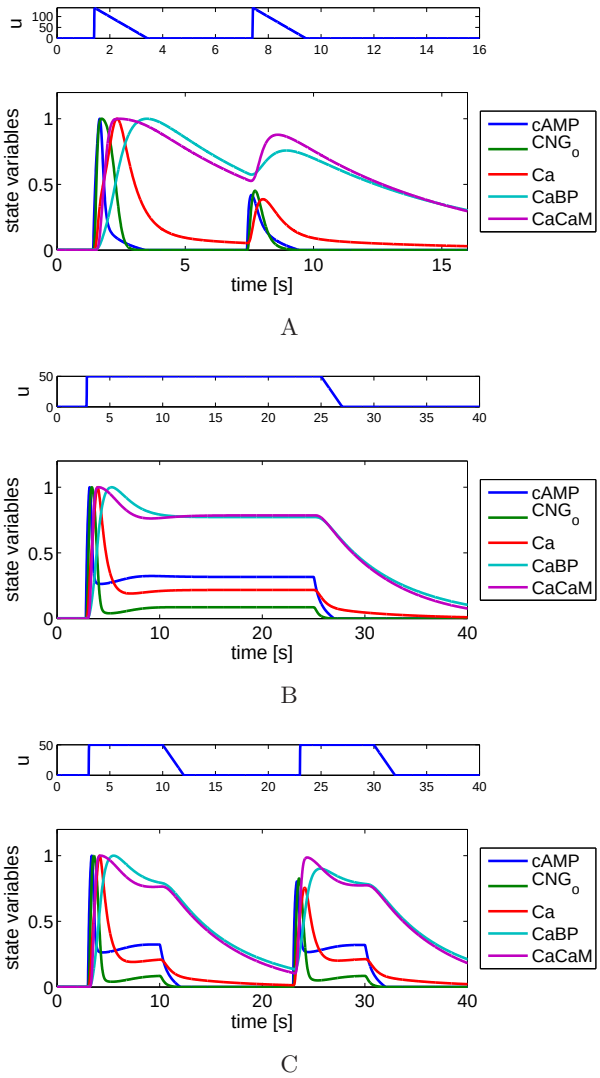

Figure S4: **Time profile of the state variables for the simulated data in response to IBMX.** Panels (A), (B) and (C) show the normalized simulation of the model in response to a paired-pulse stimulation, a prolonged stimulus, and a mixed stimulus, corresponding to the data of Fig. 4 of the main paper. The top panels on each figure represent the input given to the model.

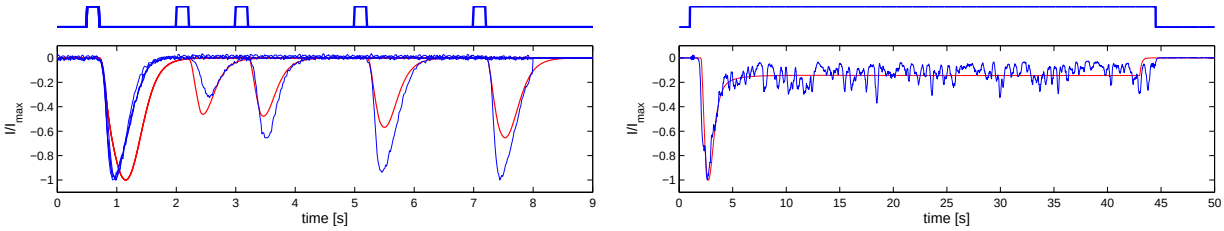

A B

Figure S5: **Adaptation in response to an odorant.** Responses of the model (red) for the data shown in Fig. S11 (blue), using the parameter set in the "common" column of Table of the paper

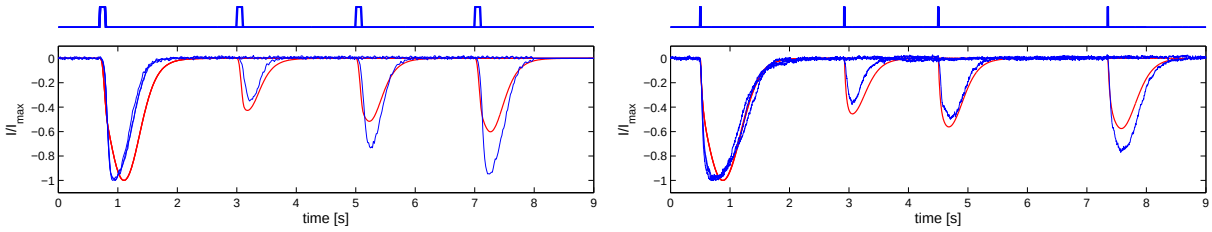

A B

Figure S6: **Adaptation in response to caged compounds.** Responses of the model (red) for the data shown in Fig. 3 (blue), using the parameter set in the "common" column of Table of the paper

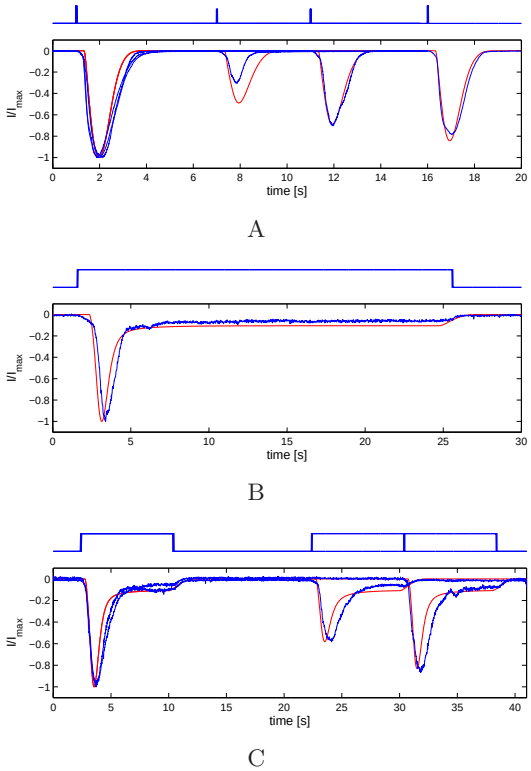

Figure S7: **Adaptation in response to IBMX.** Responses of the model (red) for the data shown in Fig. 4 (blue), using the parameter set in the "common" column of Table of the paper

First of all we tested if the parameters we obtained from the fitting procedure were in correspondence of a local minimum. We moved each parameter around its estimated value up to a 10 fold increase/decrease or until the cost function increases more than 10% of its optimum J^*. In Fig. S8 the corresponding results for the entire set of parameters are shown (J^* is plotted in red) for the case of "common" parameter set of Table in the main paper. The only two parameters for which the cost function decreases with respect to J^* are the dissociation rate λ_3 and the fractional blockage B of the CaCaM feedback in the IBMX experiments. In both cases, the variations improving on J^* are outside the range we allowed for the parameters. In particular, the lower bound we imposed in λ_3, namely 0.1, is due to the fact that in experiments a complete recovery from multipulse adaptation occurs in at most 30 s. This constrains the time constants of the feedbacks. Notice in Fig. S8 that a similar behavior does not occur for λ_2. The interpretation of this fact is straightforward: when λ_2 is kept fixed at the optimal value, the CaCaM feedback is largely redundant and it is allowed to behave as an exact integral since the CaBP feedback loop already takes care of shaping the closed-loop system as required. To confirm that this is indeed the case, we have carried out extensive simulations varying simultaneously the two dissociation rates λ_2 and λ_3 for the feedback variables. In no case did λ_2 and λ_3 assume too small values simultaneously while reproducing correctly the input-output adaptation profiles. As for the B parameter, the minimum blockage of 60% which we impose on the IBMX experiments is reasonable, given our current knowledge of the action of this blocker on PDE. Hence, in this case, the (marginal) improvement of J^* shown in Fig. S8 is to be considered non-physiological. The pattern of single parameter variations is similar on the odor experiments (B does not appear in this case) and in the IBMX data. No improvement at all appears in the 8-Br-cAMP data set.

While the local analysis carried out above is encouraging, due to the nonlinearities in the dynamics, our parameter fitting procedure is not guaranteed to find a global optimum. We tried anyway to explore the landscape of the parameter space from a more global perspective (see Fig. S9). We considered for this kind of test the parameter set obtained for the fit of the responses to odor (the behavior for the other sets is similar). For each parameter we randomly sampled rescaling factors across 4 orders of magnitude ($10^{-2} \div 10^{2}$), combining the rescaled parameters in various ways, at random. We then use these values as starting points for the parameter estimation. Fig. S9 A shows that when the procedure is repeated about 100 times a cost function smaller than J^* is never obtained. In the best suboptimal solutions we found (drawn in red in Fig. S9 A) we verified that indeed at least one of the two feedback dissociation rates is large compared to the other reaction rates. This confirms that in a model like ours the slow dynamics of the feedback is fundamental to reproduce adaptation, and supports our observation that the two feedback loops perform this task in a redundant way.

In order to evaluate how rugged the parameter landscape is, and to estimate how well our fitting procedure performs (the two aspects are linked and cannot be disentangled easily), in Fig. S9 A the initial parameter guess and the final (suboptimal) parameter set are shown connected by a line. The distance D in parameter space is calculated as

$$\mathrm{D} = ||\mathbf{p}^* - \hat{\mathbf{p}}||_2 = \sqrt{\sum_{\mathrm{i}} \left(\mathrm{p}_{\mathrm{i}}^* - \hat{\mathrm{p}}_{\mathrm{i}}\right)^2},$$

where $\mathbf{p}^*$ is the parameter vector corresponding to J^*, and $\hat{\mathbf{p}}$ the parameter vector of the current suboptimal fitting. Every segment connects a random starting point with the final result $\hat{\mathbf{p}}$ (indicated with a star in the plot). It is possible to see that a diminishing difference in the cost function

corresponds to a diminishing distance in the parameters, suggesting the idea of a landscape in the cost function with a unique region for the minimum, surrounded by a large amount of local minima at higher cost.

To increase the sample size, we repeated about 1000 times a similar procedure without re-fitting the parameters but only evaluating the cost function on a random choice of the parameters, see Fig. S9 B. For each sampled parameter vector we calculated the cost function and the distance from $\mathbf{p}^*$. No value found in this way appears below J^*, and it is possible to notice how increasing the distance in parameter space from $\mathbf{p}^*$ tends to increase the cost function, suggesting that the basin of attraction of our minimum could be quite large (thereby confirming the result of Fig. S9 A).

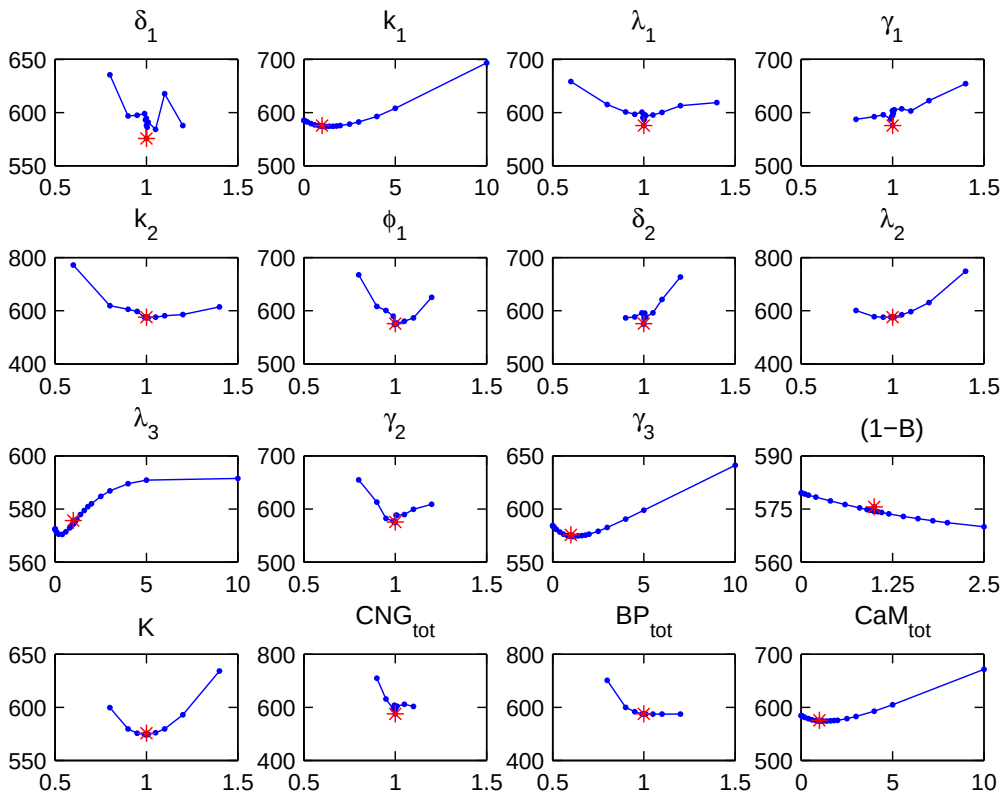

Figure S8: **Goodness of fit: testing local optimality in the neighborhood of $\mathbf{p}^*$.** Sensitivity of the cost function to single-parameter perturbations. On the x-axis the relative value of each parameter with respect to its optimal value is reported, on the y-axis the corresponding value of the cost function. $\mathbf{p}^*$ is shown in red.

Dose response relations The model presented here is able to reproduce the shift in the dynamic range caused by adaptation in the olfactory transduction pathway. The typical illustration of this feature is the dose-response curve. In this curve, the normalized maximal amplitude of the current

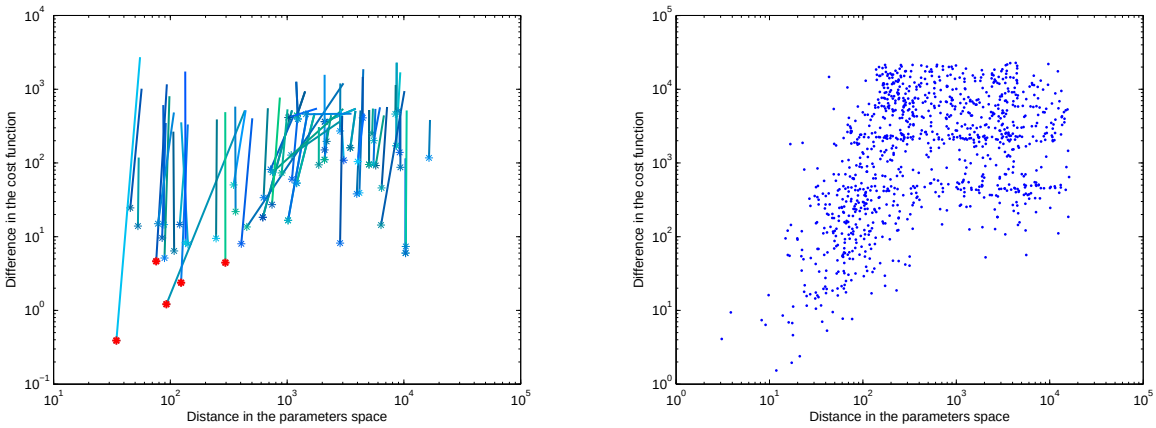

A B

Figure S9: **Goodness of fit: exploring the landscape of the cost function.** (A) Starting from random points and optimizing. On the x-axis the distance in the space of parameters is reported, on the y-axis distance from J^* of the cost function, both in a logarithmic scale. The segments connect the random starting points and the optimized $\hat{\mathbf{p}}$ (denoted with a star). The red points indicate fitting results with a difference smaller than 5 from the cost function of the optimal solution. All the $\hat{\mathbf{p}}$ very close to $\mathbf{p}^*$ in terms of cost function have similar feedback time constants as our $\mathbf{p}^*$ parameter set. (B) Evaluation of the cost function for a random choice of parameters. On the x-axis the distance in the space of parameters is reported, on the y-axis the difference in the cost function, both in a logarithmic scale.

response is plotted versus the relative input amplitude or input duration. Following adaptation, the input amplitude interval over which the curve is approximately linear (the system is responding but not saturating) is shifted and broader, allowing better detection and discrimination of further stimulations. We present here the response of our model to two different simulated stimuli. In Fig. S10 A it is possible to see the dose-response curves of the model in the case of odor stimulation (with stimulus duration on the x-axis) and in Fig. S10 B in the case of photoreleased 8-Br-cAMP (with stimulus amplitude on the x-axis). Comparing the shape of these curves with those obtained experimentally (for the type of data we are considering see [13, 2]) it is apparent that the qualitative behavior is very similar. The typical sigmoidal shape for the activation of both the control and the adapted responses, and the reduction of the distance between the two curves with increasing input are correctly reproduced. We fit these simulated data with a Hill-type function: $Y = \frac{X^n}{X^n + K_{1/2}{}^n}$ where X represents the input duration or amplitude and Y is the value of the current peak in the control or adapted state. The values for the cooperativity index n and for the half-activation constant $K_{1/2}$ are reported in Tab. S2.

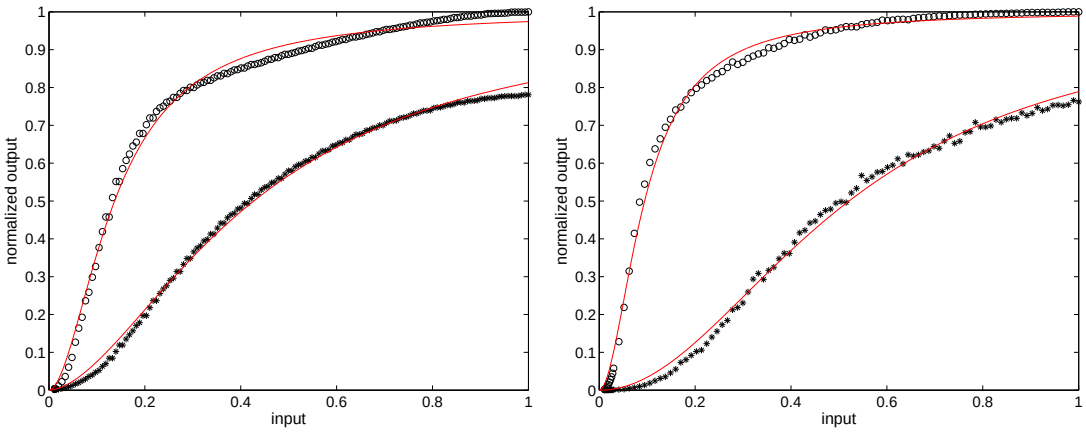

A B

Figure S10: **Dose response plot.** (A) Simulated odorant response: the black dots represent the model simulation, the red curve shows the corresponding Hill function. For the response to the first pulse, an input of increasing duration was simulated. To obtain the adapted response, the duration of the second pulse was increased, keeping fixed that of the first pulse. (B) Same as (A), but using simulated responses to a release of caged 8-Br-cAMP of increasing amplitude.

Table S2: Parameter set used to fit the dose response curves of Fig. S10.

Type of stimulation		n	$K_{1/2}$
odor	control	1.83	0.14
	adapted	1.73	0.43
8-Br-cAMP	control	1.90	0.09
	adapted	2.02	0.52

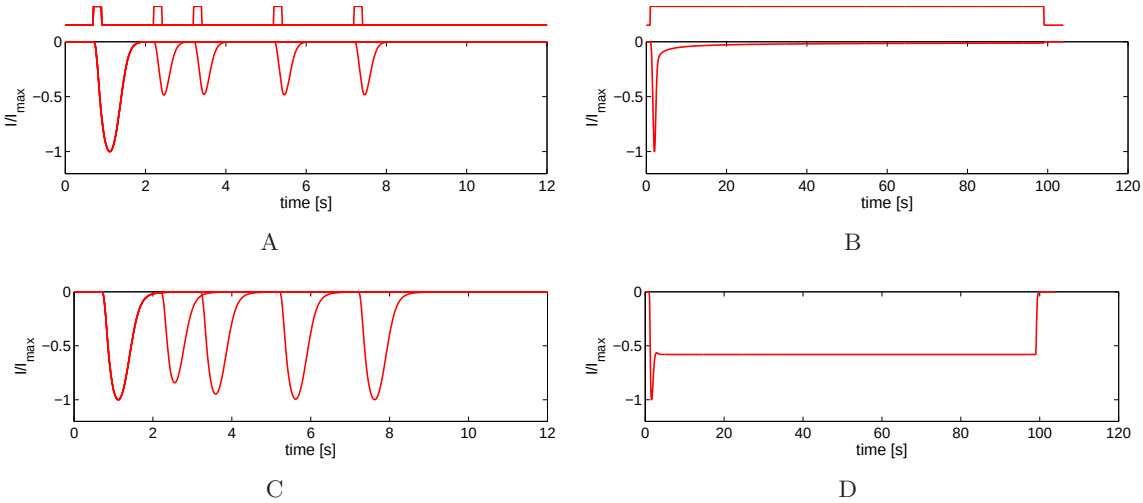

Figure S11: **Dynamical trade-off: comparison between perfect adaptation and fast dissociation of CaCaM and CaBP.** Left: Response to double pulses in the case of perfect adaptation (dissociation rates for the feedback variables, λ_2 and λ_3, equal to zero) in panel (A) and in the case of fast kinetics of the feedback variables in panel (C). The lag time for the recovery of the response is overestimated in the first case (for perfect adaptation there is no recovery) and underestimated in the second case. Right: Response to a sustained stimulation for zero (B) and fast (D) feedback kinetics rates. In the first case the pre-stimulus current recovers exactly during the stimulation (hence the name perfect adaptation) while in the second case the system adapts less than observed experimentally.

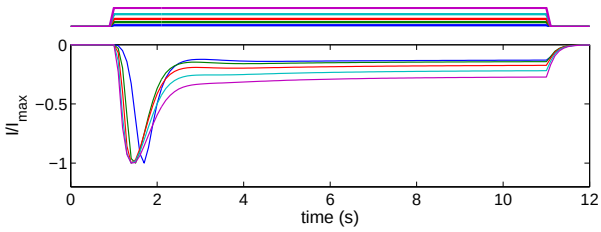

Figure S12: **Current responses to a prolonged stimulation of different amplitudes.** Responses are normalized to the amplitude of the transient peak. Increasing inputs yield increasing steady-state levels. This shows that for our model the lack of exact adaptation is not an "error" but a steady-state characteristic, incompatible with models of perfect adaptation. The green trace corresponds to the simulation in Fig. 2 of the main paper.

3 An alternative model for the CNG channel

In this section we formulate a possible alternative model for the gating of a CNG channel inspired by [19], and show that also in this case the input-output behavior is qualitatively correct. Following [19] a different formulation of the model can be considered, in which the state of a CNG channel is characterized by 3 possible conformations:

- open (hereafter $\mathrm{CNG_o}$)
- closed ($\mathrm{CNG_c}$)
- inhibited ($\mathrm{CNG_i}$)

The inhibited state of the CNG channel resembles the inactivated state of the voltage-gated Na channel, in which after depolarization, the channel is in a non-conductive state and remains refractive to further gate opening commands for a certain time interval. Although to our knowledge there is no experimental evidence to support the existence of an "inhibited" phase in CNG channels during voltage-clamp, the scheme can be used to set up a theoretical model alternative to Eqs (1)-(7) of the paper. In this scheme, the variable CaBP no longer appears: the binding of Ca to BP (permanently attached to the channel) automatically turns an open channel into an inhibited channel (second reactions of the list below). The longer time constant associated with the feedback action of the CaBP in the model (1)-(7) of the paper is replaced here by the longer time constant of the "inhibited" phase with respect to the other two phases of the CNG channel. The reactions are therefore as follows:

$$
\begin{gathered}
2\ \mathrm{cAMP} + \mathrm{CNG_c} \underset{\lambda_1}{\overset{\gamma_1}{\rightleftharpoons}} \mathrm{CNG_o} \\
\mathrm{CNG_o} + 2\ \mathrm{Ca} \xrightarrow{\gamma_2} \mathrm{CNG_i} + 2\ \mathrm{cAMP} \\
\mathrm{CNG_i} \xrightarrow{\lambda_2} \mathrm{CNG_c} + 2\ \mathrm{Ca} \\
2\ \mathrm{Ca} + \mathrm{CaM} \underset{\lambda_3}{\overset{\gamma_3}{\rightleftharpoons}} \mathrm{CaCaM} \\
\mathrm{cAMP} \xrightarrow{k_1 \cdot CaCaM + \delta_1} \mathrm{AMP}
\end{gathered}
$$

with the following conservation laws:

$$
\begin{aligned}
\mathrm{CNG_{tot}} &= \mathrm{CNG_o} + \mathrm{CNG_c} + \mathrm{CNG_i}; \\
\mathrm{CaM_{tot}} &= \mathrm{CaM} + \mathrm{CaCaM}.
\end{aligned}
$$

Adding a factor σ=volume/surface to allow the interaction between surface and volume concentrations of variables, the reactions above lead to the equations:

$$\begin{aligned}
\frac{d\mathrm{cAMP}}{dt} &= 2\cdot\frac{1}{\sigma}\cdot\lambda_1\cdot\mathrm{CNG_o} - 2\cdot\frac{1}{\sigma}\cdot\gamma_1\cdot\mathrm{cAMP}^2\cdot(\mathrm{CNG_{tot}}-\mathrm{CNG_o}-\mathrm{CNG_i}) \\
&\quad -(\mathrm{k_1}\cdot\mathrm{CaCaM}+\delta_1)\cdot\mathrm{cAMP} + 2\cdot\frac{1}{\sigma}\cdot\gamma_2\cdot\mathrm{Ca}^2\cdot\mathrm{CNG_o}+\mathrm{u} && \text{(S1)}\\
\frac{d\mathrm{CNG_o}}{dt} &= \gamma_1\cdot\mathrm{cAMP}^2\cdot(\mathrm{CNG_{tot}}-\mathrm{CNG_o}-\mathrm{CNG_i}) - \lambda_1\cdot\mathrm{CNG_o} - \gamma_2\cdot\mathrm{Ca}^2\cdot\mathrm{CNG_o} && \text{(S2)}\\
\frac{d\mathrm{Ca}}{dt} &= \phi_1\cdot\frac{1}{\sigma}\cdot\mathrm{CNG_o} - \delta_2\cdot\mathrm{Ca} - 2\cdot\frac{1}{\sigma}\cdot\gamma_2\cdot\mathrm{Ca}^2\cdot\mathrm{CNG_o} + 2\cdot\frac{1}{\sigma}\cdot\lambda_2\cdot\mathrm{CNG_i} \\
&\quad -2\cdot\gamma_3\cdot\mathrm{Ca}^2\cdot(\mathrm{CaM_{tot}}-\mathrm{CaCaM}) + 2\cdot\lambda_3\cdot\mathrm{CaCaM} && \text{(S3)}\\
\frac{d\mathrm{CNG_i}}{dt} &= \gamma_2\cdot\mathrm{Ca}^2\cdot\mathrm{CNG_o} - \lambda_2\cdot\mathrm{CNG_i} && \text{(S4)}\\
\frac{d\mathrm{CaCaM}}{dt} &= \gamma_3\cdot\mathrm{Ca}^2\cdot(\mathrm{CaM_{tot}}-\mathrm{CaCaM}) - \lambda_3\cdot\mathrm{CaCaM} && \text{(S5)}
\end{aligned}$$

Hypothesizing slow dynamics for the $\mathrm{CNG_i}$ and CaCaM variables this model is able to reproduce both types of adaptation observed in the olfactory transduction (Fig. S13). In this model, the binding of Ca to BP (and hence the initiation of the inhibition phase) coincides with the detachment of cAMP (and hence with the termination of the opening gate signal). In the model (1)-(7) of the paper, the two gating commands are instead independent and can coexist, which seems to us a more appropriate description for this population of channels. Furthermore the profile of a dose-response curve cannot be reproduced by Eqs (1)-(7). Finally the behavior in the adapted state is different in the two models. Indeed, in the case of a saturating input a model like (S1)-(S5) provides right after the stimulus a total inhibition (and unavailability) of the CNG channels. Therefore this system is unable to respond to subsequent stimuli, until the channels have turned from the inhibited to a closed state. On the contrary, in the system of Eqs (1)-(7) the CNG channels are still able to produce a response, although reduced due to the feedback action of the calcium binding protein complex.

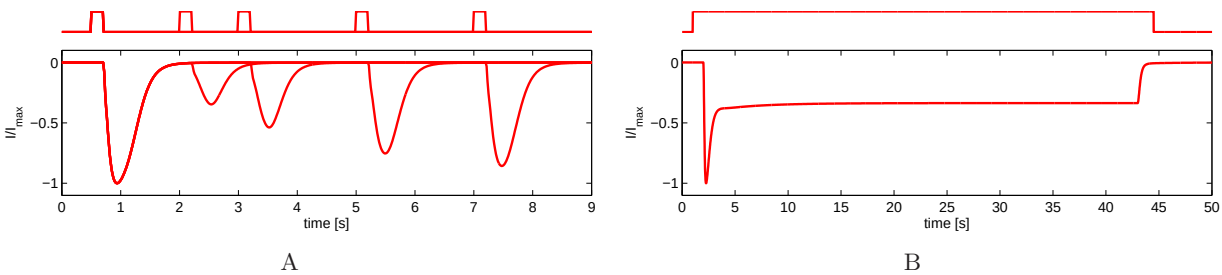

Figure S13: **3-conformation model for the CNG channel.** Panel (A) shows the response of the model of Eqs (S1)-(S5) to a double pulses protocol. Panel (B) shows the response on the same model in the case of a sustained stimulation.

Notice that also for this model in zero Ca the channels never become inhibited, hence both feedback mechanisms are absent, consistently with the experimental data.

References

[1] S Balasubramanian, J W Lynch, and P H Barry. Calcium-dependent modulation of the agonist affinity of the mammalian olfactory cyclic nucleotide-gated channel by calmodulin and a novel endogenous factor. *J Membr Biol*, 152(1):13–23, Jul 1996.

[2] A Boccaccio, L Lagostena, V Hagen, and A Menini. Fast adaptation in mouse olfactory sensory neurons does not require the activity of phosphodiesterase. *J Gen Physiol*, 128(2):171–184, Aug 2006.

[3] A Boccaccio and A Menini. Temporal development of cyclic nucleotide-gated and Ca^{2+}-activated Cl^{-} currents in isolated mouse olfactory sensory neurons. *J Neurophysiol*, 98(1):153–160, Jul 2007.

[4] F F Borisy, G V Ronnett, A M Cunningham, D Juilfs, J Beavo, and S H Snyder. Calcium/calmodulin-activated phosphodiesterase expressed in olfactory receptor neurons. *J Neurosci*, 12(3):915–923, Mar 1992.

[5] J Bradley, W Bönigk, K W Yau, and S Frings. Calmodulin permanently associates with rat olfactory CNG channels under native conditions. *Nat Neurosci*, 7(7):705–710, Jul 2004.

[6] T Y Chen and K W Yau. Direct modulation by Ca^{2+}-calmodulin of cyclic nucleotide-activated channel of rat olfactory receptor neurons. *Nature*, 368(6471):545–548, Apr 1994.

[7] S Firestein, C Picco, and A Menini. The relation between stimulus and response in olfactory receptor cells of the tiger salamander. *J Physiol*, 468:1–10, Aug 1993.

[8] T V Getchell. Functional properties of vertebrate olfactory receptor neurons. *Physiol Rev*, 66(3):772–818, Jul 1986.

[9] T V Getchell and G M Shepherd. Adaptive properties of olfactory receptors analysed with odour pulses of varying durations. *J Physiol*, 282:541–560, Sep 1978.

[10] Y Gu, P Lucas, and J P Rospars. Computational model of the insect pheromone transduction cascade. *PLoS Comput Biol*, 5(3), Mar 2009.

[11] S J Kleene. The electrochemical basis of odor transduction in vertebrate olfactory cilia. *Chem Senses*, 33(9):839–859, Nov 2008.

[12] T Kurahashi. Activation by odorants of cation-selective conductance in the olfactory receptor cell isolated from the newt. *J Physiol*, 419:177–192, Dec 1989.

[13] T Kurahashi and A Menini. Mechanism of odorant adaptation in the olfactory receptor cell. *Nature*, 385(6618):725–729, Feb 1997.

[14] L Lagostena and A Menini. Whole-cell recordings and photolysis of caged compounds in olfactory sensory neurons isolated from the mouse. *Chem Senses*, 28(8):705–716, Oct 2003.

[15] H R Matthews and J Reisert. Calcium, the two-faced messenger of olfactory transduction and adaptation. *Curr Opin Neurobiol*, 13(4):469–475, Aug 2003.

[16] D Ottoson. Analysis of the electrical activity of the olfactory epithelium. *Acta Physiol Scand Suppl*, 35(122):1–83, 1955.

[17] S Pifferi, A Boccaccio, and A Menini. Cyclic nucleotide-gated ion channels in sensory transduction. *FEBS Lett*, 580(12):2853–2859, May 2006.

[18] R Y Pun and S J Kleene. Contribution of cyclic-nucleotide-gated channels to the resting conductance of olfactory receptor neurons. *Biophys J*, 84(5):3425–3435, May 2003.

[19] J Reidl, P Borowski, A Sensse, J Starke, M Zapotocky, and M Eiswirth. Model of calcium oscillations due to negative feedback in olfactory cilia. *Biophys J*, 90(4):1147–1155, Feb 2006.

[20] D Schild and D Restrepo. Transduction mechanisms in vertebrate olfactory receptor cells. *Physiol Rev*, 78(2):429–466, Apr 1998.

[21] H Takeuchi and T Kurahashi. Mechanism of signal amplification in the olfactory sensory cilia. *J Neurosci*, 25(48):11084–11091, Nov 2005.

[22] J Wei, A Z Zhao, G C Chan, L P Baker, S Impey, J A Beavo, and D R Storm. Phosphorylation and inhibition of olfactory adenylyl cyclase by CaM kinase II in Neurons: a mechanism for attenuation of olfactory signals. *Neuron*, 21(3):495–504, Sep 1998.